Novel coatings for protecting solid oxide fuel cell interconnects against the dual-atmosphere effect

Available online at www.sciencedirect.com

ScienceDirect

journal homepage: www.elsevier.com/locate/he

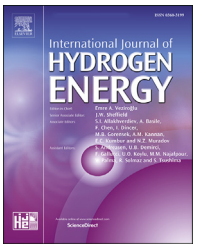

Novel coatings for protecting solid oxide fuel cell interconnects against the dual-atmosphere effect

M. Tomas[*], *A. Visibile, J.-E. Svensson, J. Froitzheim*

Energy and Materials, Chalmers University of Technology, Kemivägen 10, 41296 Gothenburg, Sweden

HIGHLIGHTS

- Coatings against hydrogen permeation are investigated for up to 7000 h.
- Al-based coatings effectively reduce the dual-atmosphere effect.
- A combined Al_2O_3//Ce/Co-coating reduces Cr evaporation and the dual-atmosphere effect.
- Al_2O_3 coatings exhibit high ASR values.

ARTICLE INFO

Article history:
Received 1 November 2022
Received in revised form
23 January 2023
Accepted 26 January 2023
Available online xxx

Keywords:
SOFC
Interconnect
Dual-atmosphere
Coating
ASR
Alumina

ABSTRACT

A key component of a Solid Oxide Fuel Cell (SOFC) is the interconnect, which connects individual fuel cells in series to form a fuel cell stack to reach a desired electrical potential. The interconnect is exposed to air and fuel in parallel, these so-called dual-atmosphere conditions give rise to especially severe corrosion on the air-side. This work investigates coatings to mitigate this effect. Physical Vapour Deposition (PVD) CeCo-coated AISI 441 samples on the air-side and PVD metallic Al- and Al_2O_3-coated AISI 441 samples on the fuel-side were exposed under dual-atmosphere conditions for up to 7000 h. The evolution of the corrosion products was followed every 1000 h with an optical microscope. Scanning electron microscopy and energy-dispersive x-ray spectroscopy were performed on cross-sections of the samples after 3000 h of exposure. The SEM analysis showed that coating on the air-side improved the sample's life-time by reducing the level of Cr evaporation even in a dual-atmosphere. The use of fuel-side coatings suppressed the dual-atmosphere effect since the coatings formed a barrier to hydrogen permeation. The best results were observed with metallic Al and Al_2O_3 coating on the fuel-side, which drastically reduced the dual-atmosphere effect. However, the poor conductivity of Al_2O_3 makes its use as a coating challenging.

Introduction

In the last few decades, Solid Oxide Fuel Cells (SOFCs) have attracted interest due to their high electrical efficiency levels (>60%), low emissions, and high fuel flexibility [1,2]. SOFCs are considered a promising technology to address the demand for more sustainable energy, as they are valid systems to convert hydrogen or hydrocarbons from renewable sources to electrical energy. However, high production costs and limited lifetimes have made commercialisation difficult. A key component of an SOFC is the interconnect (IC), which connects the

* *Corresponding author.*
E-mail address: tommat@chalmers.se (M. Tomas).

https://doi.org/10.1016/j.ijhydene.2023.01.313

individual fuel cells in series to form a fuel cell stack, so as to reach the desired electrical potential. As fuel cell operating temperatures decreased, a switch from ceramic interconnects to Ferritic Stainless Steel (FSS) interconnects became feasible. The most important parameters to consider in relation to interconnects are: material stability in relation to high-temperature oxidation; and electrical resistance of the formed oxide. When oxidised, manganese (Mn)-containing ferritic stainless steels have been shown to form a $(Cr, Mn)_3O_4$ spinel top layer on top of the semi-conductive chromia scale in the temperature range of the SOFC [3]. The use of low-cost, commercially available stainless steels, such as AISI 441, instead of tailor-made alloys may provide substantial cost savings but may also lead to faster degradation of the interconnect. Two well-known degradation processes are active when an FSS interconnect is exposed at high temperature: (a) Cr(VI) evaporation from the steel, which poisons the cathode [4]; and (b) growth of a Cr_2O_3 layer, which reduces the electrical conductivity [5,6]. In the past decade, several coatings have been studied and proposed [6–13] as a way to mitigate these two phenomena. To reduce Cr(VI) evaporation, the most-heavily commercialised examples are the Mn- and cobalt (Co)-based spinel coatings (MCO coatings), which are considered the state-of-the-art for this purpose. An alternative strategy to obtain MCO coatings is to coat the substrate with metallic Co. This Co layer will oxidise to form Co_3O_4 and becomes enriched in Mn through diffusion from the steel substrate during stack operation [7,8]. MCO coatings are highly effective, reducing Cr(VI) evaporation by a factor of more than 10 compared to uncoated samples [9]. Reactive Elements (REs) have been described by *Hou* et al. [10] as exerting beneficial effects on Cr_2O_3-forming alloys through: selective oxidation of chromium; reducing the Cr_2O_3 scale growth rate; or changing the transport mechanism from outward metal transport to inward oxygen diffusion. A clear difference in chromia thickness has been observed for samples coated with a thin layer of ceria, compared to samples without an RE layer [9,11–13].

The so-called 'dual-atmosphere effect' is another typical degradation process for SOFCs, especially when operated at intermediate temperatures [14,15]. Chromia former stainless steels like AISI 441 or Crofer 22 APU, exposed at high temperature in single air or humid hydrogen gas, form a protective scale of Cr_2O_3 with a cap of $(Mn, Cr)_3O_4$ spinel above (if the alloy contains Mn) [16]. In a single condition, the diffusion of Cr toward the surface is faster than its consumption (scale growth and Cr evaporation) so the formation of the scale is ensured. Once a sample is exposed on one side to air, and on the other side to hydrogen (dual-atmosphere conditions), the outcome largely changes. *Yang* et al. [17,18] noticed that an alloy exposed to a dual environment behaves differently from one exposed to a single atmosphere. Although it has been addressed that diffused hydrogen from the fuel-side affects the air-side oxidation, the mechanism behind the protective oxide scale breakdown is not fully clear. Moreover, the severity of the dual-atmosphere effect varies widely among studies [19–22]. At high temperatures (800 °C–850 °C), several authors [17,18,23,24] noticed an iron enrichment of the protective scale on the air-side. At lower temperatures (600 °C –700 °C) the air-facing side of the sample undergoes severe corrosion with the formation of hematite nodules and later formation of a thick hematite scale [15,25,26]. Iron oxides are not protective, thus, the scale grows several orders of magnitude faster than chromium oxide leading to faster material degradation and loss of performance. This effect was found on various alloys [27] like AISI 441 [14,19,28], AISI 430 [29,30], Sanergy HT [31], AISI 444 [32] and Crofer APU 22 [33], to cite the most used ones in terms of interconnect applications. Other authors [18,26,34,35] have stated that a beneficial effect of a higher Cr concentration in the alloy may help reduce the dual-atmosphere effect. Several explanations have been proposed to explain this phenomenon. *Rufner* et al. [21] suggested that the pO_2 on the air-side could be locally modified by the permeated hydrogen. *Yang* et al. [18] instead pointed out that it may be due to an increased number of cation vacancies close to the air-side, which leads to hydroxide species formation that enhances scale growth rate. Other authors [36,37] proposed theories in which the lattice is distorted because of hydrogen presence. Recently *Gunduz* et al. [15] showed how the hydrogen diffusion into the alloy might affect the Cr diffusion, thus promoting non-protective Fe-oxide formation. *Goebel* et al. [38] have shown that thicker steel sheets reduce the ingress of hydrogen to some extent.

However, in those studies, the samples were not coated. Previous research [39] has demonstrated the effect of Ce/Co-coated samples exposed to a dual-atmosphere at 850 °C. It has been established that Ce/Co coating helps to mitigate the dual-atmosphere effect at higher operating temperatures. However, samples exposed at 600 °C suffer severe corrosion after a short period of time. This is in accordance with previous research that described the inverse temperature effect [19].

While air-side coatings have been extensively studied, there are only very few studies on fuel-side coatings. Some studies [40,41] show the efficiency of Y-based coatings in a reducing environment with high humidity by the formation of a stable $YCrO_3$ phase that is electrically conductive. Another study [42] described ceria as potential fuel side coating with good electrical conductivity for SOFC application. Ceria seems to inhibit the interdiffusion processes between the ferritic steel and the Ni-anode. Ni-coatings has been studied, on Crofer 22H in fuel environment, leading to the formation of different Cr-rich oxides formed within the Ni layer [43]. Other studies on Fe–22Cr steels show the formation of an austenitic phase, caused by the diffusion of Ni within the substrate, reducing the growth rate of the chromia layer [44].

However, to the best of our knowledge, no previous studies were performed in dual-atmosphere conditions with hydrogen-barrier coatings on the fuel-side.

The main indication for the efficiency of fuel-side coatings in dual-atmosphere conditions comes from *Goebel* et al. [28], who examined the effect of pre-oxidation time and location and showed that an oxide scale on the fuel-side is particularly effective in mitigating the dual-atmosphere effect.

In the present work, barrier coatings developed to reduce the dual-atmosphere corrosion for Intermediate-Temperature Solid Oxide Fuel Cells (IT-SOFCs) are presented for the first time. The state-of-the-art Ce/Co coating on the air-side is

Please cite this article as: Tomas M et al., Novel coatings for protecting solid oxide fuel cell interconnects against the dual-atmosphere effect, International Journal of Hydrogen Energy, https://doi.org/10.1016/j.ijhydene.2023.01.313

exposed in combination with novel coatings on the fuel-side: metallic Al and Al_2O_3 deposited via Physical Vapour Deposition (PVD). Coating the fuel-side is expected to reduce the ingress of hydrogen into the alloy and to reduce the dual-atmosphere effect on the air-side. Uncoated samples that are pre-oxidised for 5 h at 800 °C are exposed as a reference. All the coatings are exposed under simulated SOFC working conditions for 3000 h.

Materials and methods

Dual-atmosphere set-up

To simulate dual-atmosphere conditions, steel samples were simultaneously exposed in air +3% H_2O on one side and Ar − 5% H_2 − 3% H_2O on the other side, at 600 °C. All the experiments were conducted in a dual-atmosphere using the experimental set-up described by *Alnegren* et al. [14]. The sample holder construction is based on a design by Montana State University, and further information on this set-up can be found elsewhere [21]. Gold rings were used to seal the circular samples to the set-up, to ensure gas-tightness.

Sample characteristics and preparation

The compositions and characteristics of the materials used in this study are described in Table 1 and Table 2.

Samples were coated by Sandvik Materials Technology AB using a proprietary PVD process. Coin-shaped samples (Ø 21 mm) were stamped out of a metal sheet using a hydraulic press. The experimental matrix and exposure characteristics are listed in Table 2. A cleaning procedure that consisted of washing for 20 min in acetone and 20 min in ethanol was performed before any thermal treatment. All the samples were then pre-oxidised at 800 °C ± 5 °C for 5 h in air +3% H_2O with a ramp rate of 1 °C·min^{-1}, under a flow of 280 mL·min^{-1}.

Exposures

All samples were exposed to a humid dual-atmosphere. The following gases were used: Ar - 5% H_2 − 3% H_2O with a flow rate of 120 smL·min^{-1} on the fuel-side; and air +3% H_2O with a flow rate of 8800 smL·min^{-1} on the air-side. This resulted in an airflow speed of around 27 cm·s^{-1} inside the quartz tube; therefore, kinetically controlled, flow-independent chromium evaporation rates were achieved [46]. To adjust the humidity level to 3%, all gases were bubbled through water baths with temperature-controlled reflux condensers set to 24.4 °C. All exposures were conducted at a temperature of 600 °C ± 5 °C. A ramp of 1 °C·min^{-1} was used to heat up and cool down the samples, to minimize oxide spallation. The exposure was interrupted after 500 h, 1000 h, 2000 h, and 3000 h, to document the evolution of the oxide scale. Selected samples were exposed for up to 7000 h to assess life-time. All the experiments involving exposure for 3000 h were repeated to ensure data reproducibility.

Microscopy

Photographs of the samples were taken at different exposure times using a Nikon SMZ800 camera equipped with a ring light. For the cross-section analyses, the samples were cut with an oil-free, low-speed saw (Struers Minitom). Cross-sections of all the samples were then prepared using a Leica EM TIC 3X Broad Ion Beam (BIB) with an acceleration voltage of 8 kV and a current of 3 mA. The resulting cross-sections were analysed using the JEOL 7800F Prime SEM. Imaging was performed with an acceleration voltage of 10 kV, and Energy-Dispersive x-ray (EDX) analysis was performed with an acceleration voltage of 15 kV.

Area-specific resistance (ASR) measurement

To determine the ASR contribution of the fuel side coatings selected samples were pre-oxidised accruing to the procedure described above and subsequently exposed for 168 h in Ar − 5% H_2 + 3% H_2O at 600 °C. The ASR is the measured resistance

Table 1 − Compositions of the studied alloys (in wt%), as specified by the manufacturer.

Materials	Fe	Cr	C	Mn	Si	Ni	Ti	Nb	Al	N	P	S
AISI 441 Thickness: 0.3 mm Batch: 89,893	Bal.	17.53	0.016	0.40	0.59	0.15	0.172	0.41	0.007	0.015	0.024	<0.001

Table 2 − Experimental matrix of the materials used and their exposure times.

Materials	Coating		Exposure time (h)
	Fuel-side	Air-side	
AISI 441	Al_2O_3 (~500 nm)	Uncoated	3000
AISI 441	Al (~1000 nm)	Uncoated	3000
AISI 441	Al (~1000 nm)	10 nm Ce/600 nm Co	7000
AISI 441	Uncoated	10 nm Ce/600 nm Co	3000
AISI 441	Uncoated	Uncoated	3000

Al coating is protected by the patent number: *EP3256617B1* [45].

Please cite this article as: Tomas M et al., Novel coatings for protecting solid oxide fuel cell interconnects against the dual-atmosphere effect, International Journal of Hydrogen Energy, https://doi.org/10.1016/j.ijhydene.2023.01.313

(R) multiplied by the contact area (A). A sputter mask with dimensions of 10 × 10 mm^2 was placed on the sample, which was then coated with gold for 30 min using the Quorum 150 sputter coater and a sputtering current of 60 mA. This procedure was repeated for the reverse side of the sample. The sputtering step was used to produce electrodes with a defined area and to ensure good contact between the sample and the platinum electrodes. The exposed samples were then mounted in a ProboStat™ (NorECs, Norway) measurement set-up using a 1 cm^2 Pt wire and grid to contact the sample electrodes. The resistance was measured by the 2-point, 4-wire method at 600 °C in air. The ASR was measured in Ar − 5% H_2 + 3% H_2O for 1 h. During the subsequent cooling of the sample, the ASR was monitored too to check for semiconductive behaviour. The uncoated side of the sample was ground before the Au sputtering to minimize the contribution of the uncoated side of the sample. Hence, the obtained values were not divided by two.

Results & discussion

Visualisation of the dual-atmosphere effect throughout the exposure

Fig. 1 shows the evolution of all the samples exposed for up to 3000 h to the dual-atmosphere conditions. During the first 500 h, there are no apparent signs of severe corrosion. The protective behaviour is attributed to the long duration of pre-oxidation treatment (5 h at 800 °C), in line with the earlier works of *Goebel* et al. [28] and *Reisert* et al. [47], which showed a direct relationship between the length of the pre-oxidation step and the onset of breakaway corrosion. Nevertheless, after 1000 h of exposure, the uncoated and Ce/Co-coated samples show signs of breakaway corrosion, while the other samples remain protective. The Ce/Co-coated sample appears to be slightly more protective than the uncoated sample. However, once the sample experiences 2000 h of exposure, the Ce/Co-coated sample exhibits corrosion comparable to that of the uncoated sample. The samples with fuel-side coatings still show no visible sign of breakaway corrosion at this point. After 3000 h of exposure, the uncoated and Ce/Co-coated samples display similar levels of corrosion, while the samples coated on the fuel-side do not show visible signs of breakaway oxidation and seem to behave in a similar manner. Nevertheless, as will be discussed below, their conditions are highly different.

The efficiency of the Ce/Co coating in terms of delaying corrosion has been demonstrated previously in a single atmosphere [9,11,12]. On the other hand, coatings of the fuel-side are expected to act as a barrier to the ingress of hydrogen in a manner similar to that shown for pre-oxidation [48,49].

Microstructural analysis

Uncoated sample exposed for 3000 h

Fig. 2 shows the SEM micrographs of the uncoated sample. The top-view of the air-side (see Fig. 2a) and the fuel-side (see Fig. 2b) after pre-oxidation, depict a homogeneous oxide scale

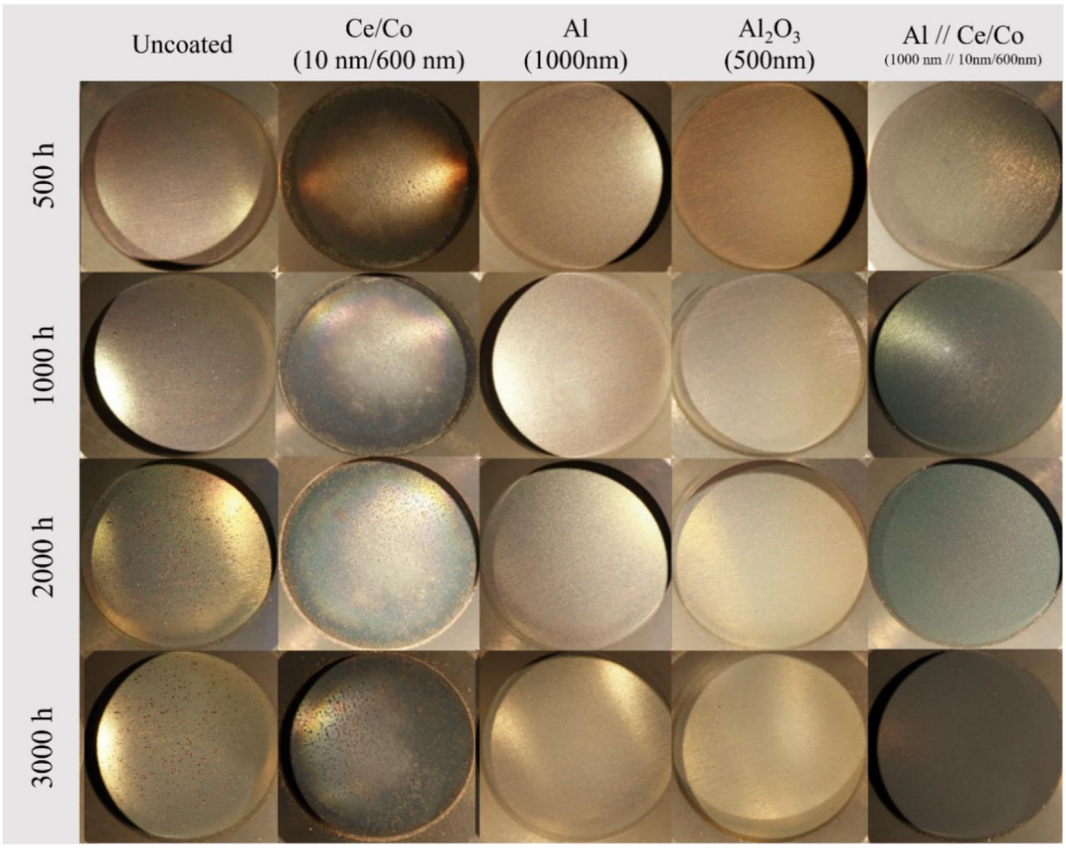

Fig. 1 − Photographs of the air-facing sides of AISI 441 coupons taken during exposure to a discontinuous dual-atmosphere (Ar-5% H_2 + 3% H_2O//Air + 3% H_2O) at 600 °C.

Please cite this article as: Tomas M et al., Novel coatings for protecting solid oxide fuel cell interconnects against the dual-atmosphere effect, International Journal of Hydrogen Energy, https://doi.org/10.1016/j.ijhydene.2023.01.313

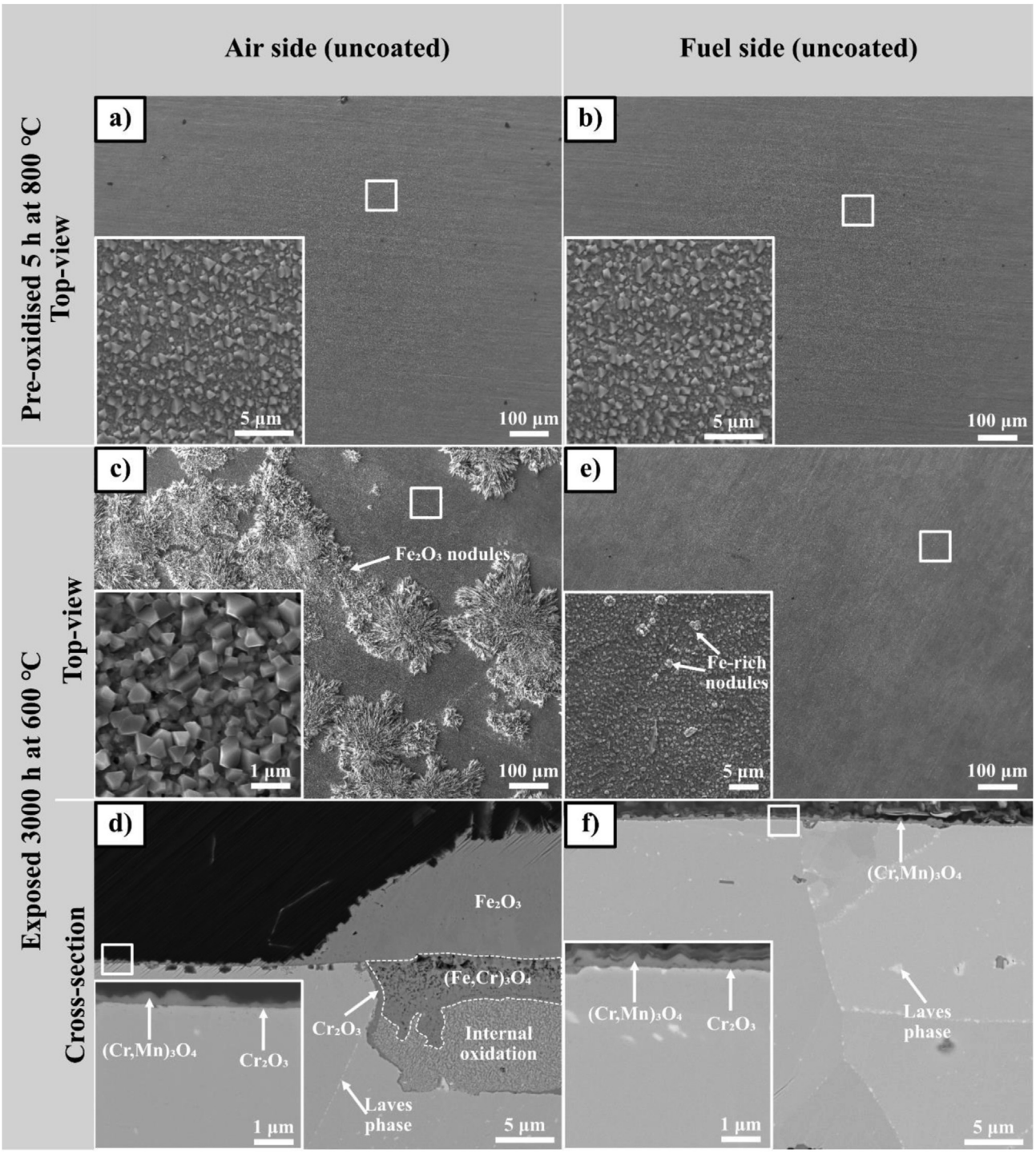

Fig. 2 – SEM micrographs representing: a) top-view of the air-side of the pre-oxidised sample; b) top-view of the fuel-side of the pre-oxidised sample; c) top-view of the air-side; d) cross-section of the air-side; e) top-view of the fuel-side; and f) cross-section of the fuel-side of 441 uncoated samples pre-oxidised for 5 h exposed to the dual-atmosphere (Ar-5% H_2 + 3% H_2O// Air + 3% H_2O) for 3000 h at 600 °C. Inset: higher-magnification image of selected scale regions.

covering the sample. No visible signs of breakaway oxidation can be observed on any of the samples after any of the exposures.

After 3000 h of exposure, the air-side of the uncoated sample exhibits a surface that is partially covered with hematite nodules (see Fig. 2c) that are roughly 300 µm in width. On top of these nodules, whiskers can be observed. Previous studies [21,29] have also documented the presence of hematite nodules on 430 and 441 steel samples exposed to similar dual-atmosphere conditions. A protective oxide is observed between the nodules. The cross-section of the air-side (Fig. 2d) confirms the observations made from Fig. 2c, showing a

Please cite this article as: Tomas M et al., Novel coatings for protecting solid oxide fuel cell interconnects against the dual-atmosphere effect, International Journal of Hydrogen Energy, https://doi.org/10.1016/j.ijhydene.2023.01.313

nodule of Fe_2O_3 and a thin (<1 μm) protective oxide scale comprised of (Cr, Mn)$_3O_4$ spinel and chromia. According to previous research [14,50], this layer is mainly composed of (Cr, Mn)$_3O_4$ spinel and chromia. The thickness of the breakaway corrosion product is about 25 μm as a result of the poor protective behaviour of the iron-rich oxide. Beneath the Fe_2O_3 nodule, a (Fe, Cr)$_3O_4$ spinel layer is present, and an internal oxidation zone (IOZ). This degradation morphology has been reported in previous studies [14,15]. The top-view micrograph of the fuel-side (see Fig. 2e) depicts an oxide scale covering the sample's surface, together with the presence of extremely small nodules (~2 μm) following the rolling direction. This morphology is very similar to that observed after pre-oxidation (see Fig. 2b). The cross-section of the fuel-side (Fig. 2f) exhibits a protective, thin, dense, and homogeneous oxide scale, which has been identified as containing a (Cr, Mn)$_3O_4$ spinel and chromia.

Those observations accord with those made in previous studies [14,28] showing that uncoated AISI 441 ferritic stainless steel suffers severe corrosion after 1000 h of exposure at 600 °C to the dual-atmosphere, even when it is pre-oxidised for 280 min. Fe-rich nodules are identified on the surface of the air-facing side of the sample. The pre-oxidation step aims to simulate the conditioning of the stack before operation. Furthermore, it is expected to provide a protective Cr_2O_3 layer that acts as a diffusion barrier to both oxidation of the alloy and the transport of hydrogen from the fuel-side to the air-side [18,28]. *Kurokawa* et al. [51] exposed Fe−16Cr steel at 800 °C and showed that after a continuous chromia layer has formed, the permeation of hydrogen was drastically reduced by four orders of magnitude.

10 nm Ce/600 nm Co-coated sample exposed for 3000 h

Fig. 3 depicts SEM micrographs of the Ce/Co-coated sample. The plan-view of the air-side after pre-oxidation (see Fig. 3a) shows a fully protective Co spinel covering the surface of the sample. No signs of breakaway corrosion are observed. The top-view of the fuel-side (uncoated) after the pre-oxidation treatment (see Fig. 3b) exhibits an oxide scale that covers the entire surface of the sample, with no visible signs of breakaway corrosion.

After 3000 h of exposure, the air-side of the sample exhibits some iron-rich nodules that are roughly 150 μm in width with whiskers on top, while the largest part of the surface is covered by a thin protective oxide scale (see Fig. 3c), similar to that observed after pre-oxidation. There are no signs of spallation of the oxide scale on the sample, indicating good adherence of the oxidised coating. The cross-section of the air-side of the sample is shown in Fig. 3d, and two different microstructures are evident: the nodules and the protective scale. The nodule consists of three distinct layers. The top layer comprises an (Fe, Co)$_3O_4$ spinel. EDS analysis shows that the top layer contains Fe (~20 at%), Co (~10 at%), and a low percentage of Cr (~5 at%). In this case, it appears that Fe diffused within the oxide scale even with the presence of a ceria layer. Underneath this layer, an Fe-rich oxide with thickness of about 20 μm is found. Below the original sample surface, there is an (Fe, Cr)$_3O_4$ spinel with thickness similar to that of the Fe-rich oxide phase observed previously. The overall thickness of the nodules is approximately 40 μm. The nodules are fewer but more localised and thicker than those observed in uncoated samples. The protective oxide scale comprises a very thin (~100 nm) (Co,Cr)$_3O_4$ spinel on top, which contains 10 at% of Co and 10 at% of Cr, followed by 1-μm-thick Co_3O_4 spinel with a thin (~200 nm) Cr_2O_3 layer. The presence of Cr in the top layer is attributed to Cr evaporation from the sample holder. *Skilbred* et al. [39] observed similar cubic-shaped grains on the top layer of Ce/Co-coated samples exposed to dual-atmosphere conditions at 850 °C,. Furthermore, in their study, the cross-section depicts a thin Co_3O_4 layer followed by a thin Cr_2O_3 oxide scale. However, there are no signs of Fe-rich nodules. This is mainly attributed to the less-severe dual-atmosphere at high temperatures, as well as the short exposure time (150 h), which did not allow sufficient time for the breakaway [15]. Fig. 3e depicts the top-view of the fuel-side of the sample exposed to H_2 + 3% H_2O, where some small nodules (~2 μm) are present. The surface state is identical to that observed right after the pre-oxidation step (see Fig. 3b) and similar to that of the uncoated sample (Fig. 2f). From the top-view analysis, these nodules appear to have grown underneath the top layer and do not seem to promote the breakdown of the oxide scale. Fig. 3f represents the cross-section of the fuel-side. The image shows a very thin (~100 nm), dense, and homogeneous (Cr, Mn)$_3O_4$ spinel and chromia layer. A similar morphology was observed by *Niewolak* et al. [3].

The superior resistance to the dual-atmosphere effect of the Ce/Co-coated sample, as compared to the uncoated sample, is in line with previous findings [11,12,52,53] for samples exposed to a single atmosphere. It has been shown that regardless of whether the top layer is Co_3O_4, (Co, Mn)$_3O_4$ or (Co, Mn, Fe)$_3O_4$, the Cr evaporation rate at 650 °C is significantly lower for Ce/Co-coated materials than for uncoated FeCr steel. Thus, the depletion of Cr from Ce/Co-coated materials over time is less extensive than from uncoated samples, which is expected to result in less-severe breakaway oxidation.

Aluminium (~1000 nm)-coated sample exposed for 3000 h

Fig. 4 shows the SEM micrographs of the sample with Al coating on the fuel-side. After pre-oxidation, the uncoated air-side of the sample (see Fig. 4a) reveals a surface that is partially covered with small nodules, following the rolling direction of the sample. On top of these small nodules, some "plate-shaped" features, roughly 5 μm in width, can be observed. Between these small nodules, an oxide scale, similar to the one observed for the uncoated sample (see Fig. 2a), is present. The fuel-facing side of the sample (see Fig. 4b) depicts a surface that is fully covered with Al-rich oxide, with no visible signs of corrosion products.

After 3000 h of exposure, the air-side of the sample is still covered with small nodules (see Fig. 4c) that seem to be aligned with the rolling direction of the steel sheet. These nodules are much smaller than those on the uncoated and Ce/Co-coated samples, which explains they were not visible in the optical overview image (see Fig. 1). On top of these nodules, "plate-shaped" features can be seen, which differ from the whiskers present on the uncoated and Ce/Co-coated samples. A protective oxide is present between the nodules. The morphology is identical to that observed after pre-oxidation (see Fig. 4a), which indicates that the Al coating is protective against hydrogen permeation. Fig. 4d depicts the

Please cite this article as: Tomas M et al., Novel coatings for protecting solid oxide fuel cell interconnects against the dual-atmosphere effect, International Journal of Hydrogen Energy, https://doi.org/10.1016/j.ijhydene.2023.01.313

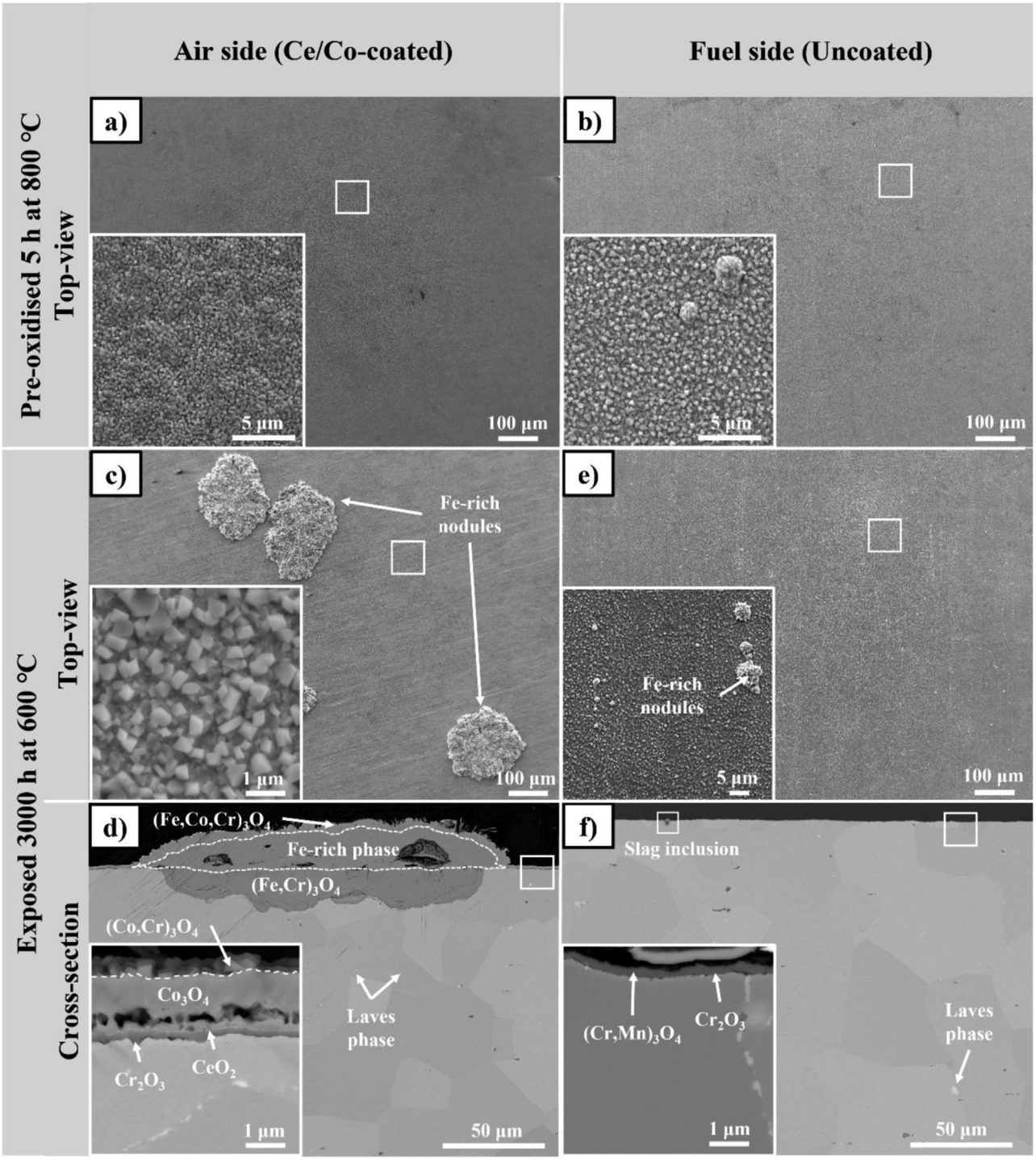

Fig. 3 – SEM micrographs representing: a) top-view of the air-side of the pre-oxidised sample; b) top-view of the fuel-side of the pre-oxidised sample; c) top-view of the air-side; d) cross-section of the air-side; e) top-view of the fuel-side; and f) cross-section of the fuel-side of the 10 nm Ce/600 nm Co-coated 441 sample exposed to the dual-atmosphere (Ar-5% H_2 + 3% H_2O// Air + 3% H_2O) for 3000 h at 600 °C. Inset: higher magnification of selected scale regions.

cross-section of the air-side of the sample. The outer part of each small nodule consists of Fe_2O_3. These nodules appear to be thinner (~5 µm) than the nodules observed in the uncoated (~25 µm) and Ce/Co-coated (~40 µm) samples. Beneath the nodules, an $(Fe, Cr)_3O_4$ spinel was identified by EDS analysis. The protective layer present between the nodules is composed of a $(Cr, Mn)_3O_4$ spinel layer followed by a Cr_2O_3 layer. The protective scale is dense, homogeneous, and approximately 200 nm in thickness, similar to the scale reported for the uncoated sample. The plan-view of the fuel-side (see Fig. 4e) depicts an Al-rich oxide phase that covers the entire surface of the sample, identical to that observed after pre-oxidation. The

Please cite this article as: Tomas M et al., Novel coatings for protecting solid oxide fuel cell interconnects against the dual-atmosphere effect, International Journal of Hydrogen Energy, https://doi.org/10.1016/j.ijhydene.2023.01.313

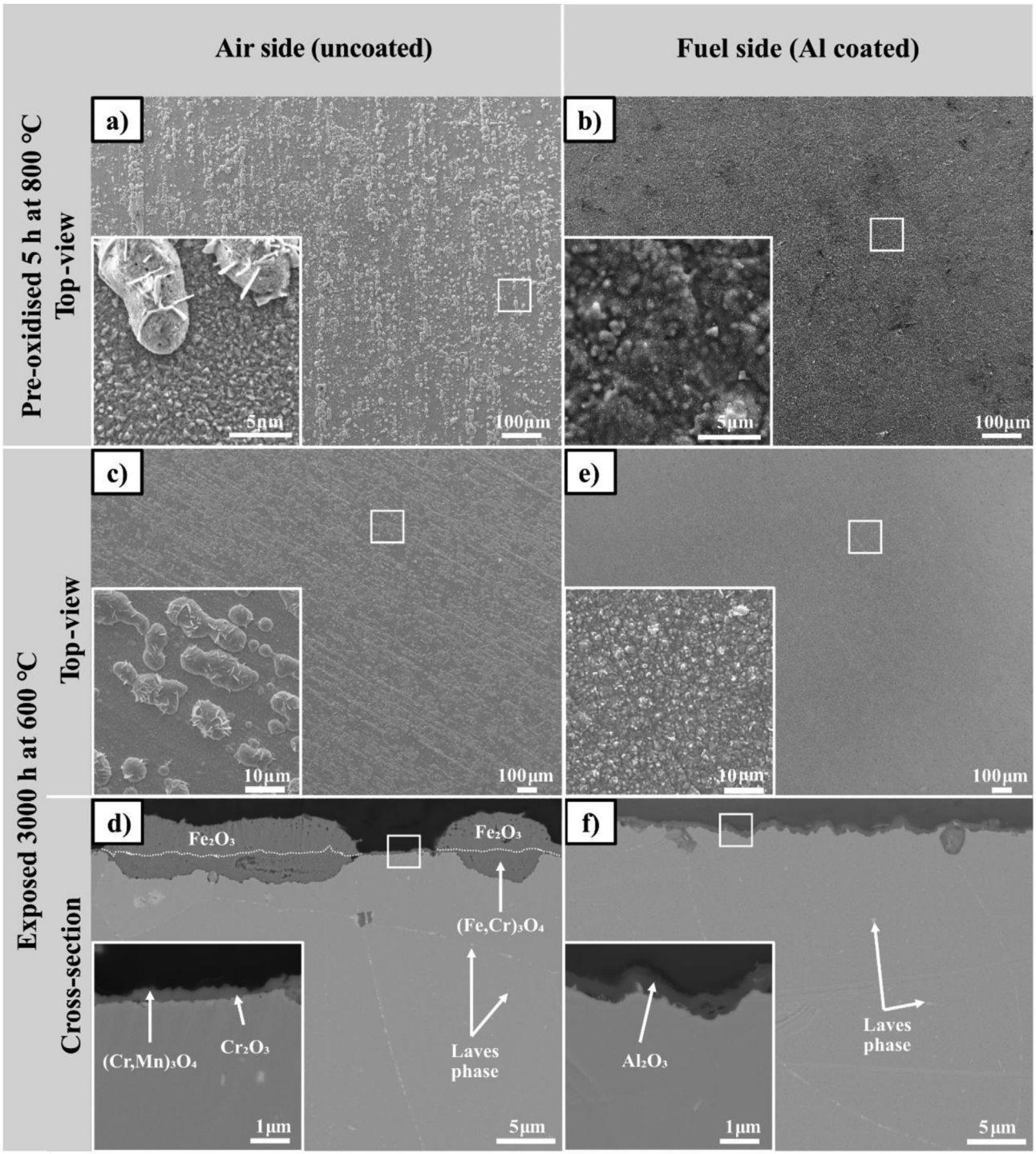

Fig. 4 – SEM micrographs representing: a) top-view of the air-side of the pre-oxidised sample; b) top-view of the fuel-side of the pre-oxidised sample; c) top-view of the air-side; d) cross-section of the air-side; e) top-view of the fuel-side; and f) cross-section of the fuel-side of the 441 aluminium (~1000 nm)-coated sample exposed to the dual-atmosphere (Ar-5% H_2 + 3% H_2O//Air + 3% H_2O) for 3000 h at 600 °C.Inset: higher magnification of selected scale regions.

metallic aluminium coating has been oxidised during the pre-oxidation (5 h) step to an Al-rich oxide phase. The cross-section of the fuel-side (see Fig. 4f) exhibits a very thin and homogeneous Al-rich scale. The surface is wavy, although the layer thickness is homogeneous at around 500 nm. X-ray diffractometry showed that it is γ-Al_2O_3 phase (not shown). The coating thickness was 1000 nm, which upon oxidation to Al_2O_3 would have generated a layer thickness of around 1300 nm. Therefore, some Al is "lost", which will be discussed in more detail below. No signs of spallation of the oxide scale have been recorded for the sample, indicating good adherence of the oxidised coating.

Please cite this article as: Tomas M et al., Novel coatings for protecting solid oxide fuel cell interconnects against the dual-atmosphere effect, International Journal of Hydrogen Energy, https://doi.org/10.1016/j.ijhydene.2023.01.313

Aluminium (~1000 nm)//10 nm Ce/600 nm Co-coated sample exposed for 7000 h

Fig. 5 shows the SEM micrographs of the Al//Ce/Co-coated sample that were exposed for 7000 h in dual-atmosphere conditions. After the pre-oxidation step, the air-facing side of the sample (see Fig. 5a) shows a protective Co-rich oxide that covers the entire surface and the presence of small nodules (~5 μm-thick) located under the oxide scale. The fuel-side of the sample (see Fig. 5b) depicts a surface fully covered with an Al-rich oxide.

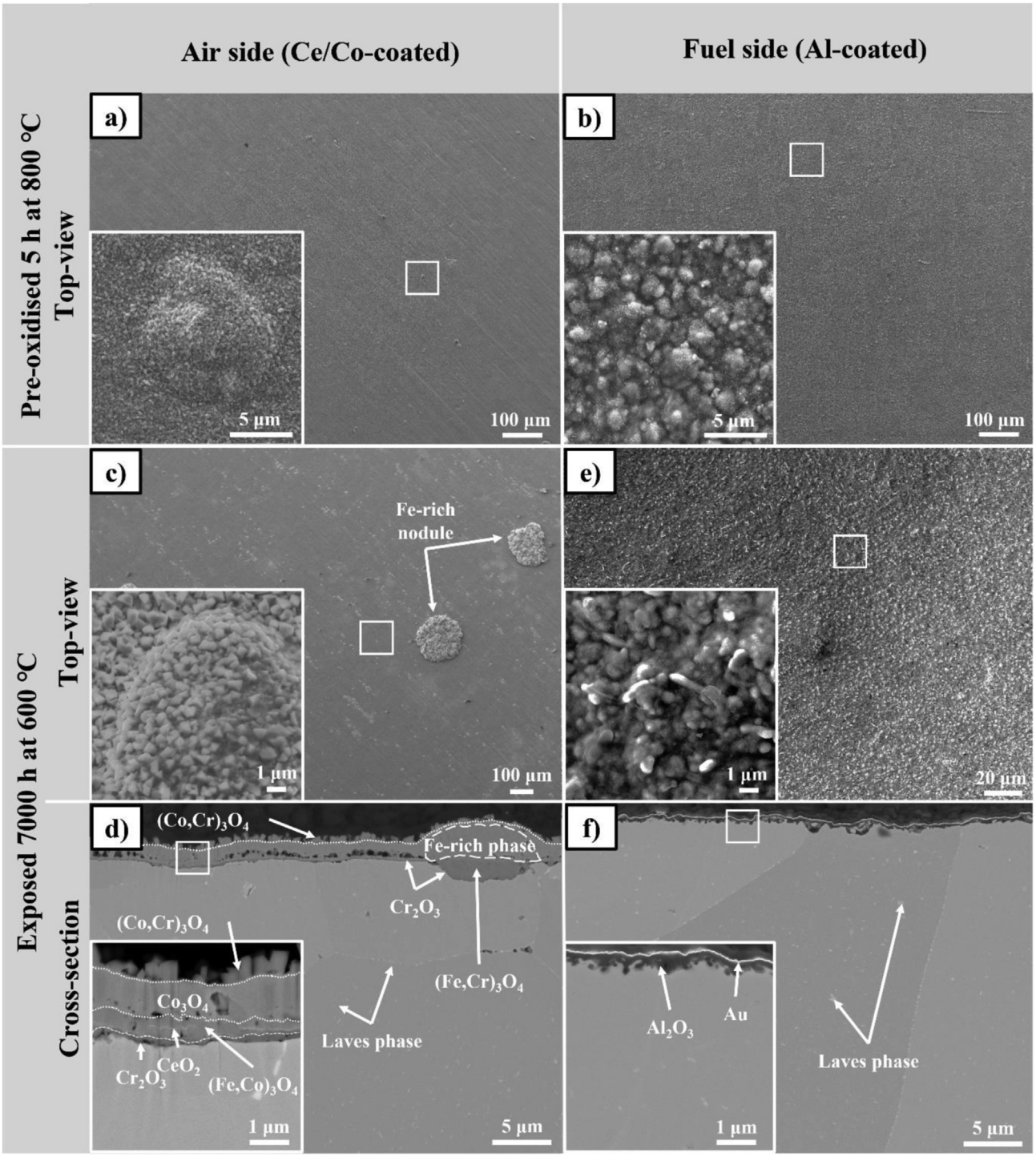

Fig. 5 – SEM micrographs representing: a) top-view of the air-side of the pre-oxidised sample; b) top-view of the fuel-side of the pre-oxidised sample; c) top-view of the air-side; d) cross-section of the air-side; e) top-view of the fuel-side; and f) cross-section of the fuel-side of the 441 sample with Al-coating on the fuel-side and Ce/Co-coating on the air-side, exposed to the dual-atmosphere (Ar-5% H_2 + 3% H_2O//Air + 3% H_2O) for 7000 h at 600 °C. Inset: higher magnification of selected scale regions. An Au layer was sputtered on the fuel-side to increase the contrast of the cross-section.

Please cite this article as: Tomas M et al., Novel coatings for protecting solid oxide fuel cell interconnects against the dual-atmosphere effect, International Journal of Hydrogen Energy, https://doi.org/10.1016/j.ijhydene.2023.01.313

A longer exposure time was selected for this specific sample because optically it appeared to be completely protective after 3000 h. The top-view of the air-side of the sample (see Fig. 5c) shows the presence of a few large Fe-rich nodules, comparable to the nodules observed on the Ce/Co-coated samples (see Fig. 3c). The nodules are of equivalent size and are present at the same frequency in the two samples. Smaller nodules are visible and seem to be covered by an oxide scale and follow the rolling direction, as previously observed after pre-oxidation (see Fig. 5a). The cross-section of the air-side (see Fig. 5d) shows two different microstructures: a homogeneous 4-layer microstructure and a small-nodule microstructure. The outer layer of the homogeneous part consists of a (Cr, Co)$_3$O$_4$ spinel that contains approximately 19 at% of Cr and 15 at% of Co. The Cr in the top layer is believed to originate from the sample holder, which is a chromia former steel. The second layer consists of an almost-pure Co_3O_4 spinel that contains roughly 4 at% of Fe. The third layer is a (Fe,Co)$_3$O$_4$ spinel with 14 at% of Fe, 14 at% of Co, and low percentages of Cr and Mn (6 at% and 3 at%, respectively). Closest to the metal, a thin Cr_2O_3 layer is present. Overall, this 4-layer microstructure appears to be porous and is roughly 1 μm-thick. The second part consists of Fe-rich small nodules located underneath a (Co,Cr)$_3$O$_4$ spinel, and beneath this, a (Fe,Cr)$_3$O$_4$ spinel is present. The small-nodule morphology on the air-side of the Al//Ce/Co-coated sample differs from the morphology of the small nodules observed on the Ce/Co-coated sample, since an oxide layer covers them. The top-view of the fuel-side (see Fig. 5e) does not show visible signs of severe corrosion and has the same morphology as that observed after pre-oxidation. The Al-rich layer is homogeneous and covers the sample. Fig. 5f depicts the cross-section of the fuel-side. As specified in Table 2, the oxide scale is much thinner than the nominal coating thickness (1000 nm) and is less homogeneous as that observed on Al-coated sample. No signs of spallation of the oxidised coatings have been noted, indicating good adherence.

Al_2O_3 (~500 nm)-coated sample exposed for 3000 h

Fig. 6 shows the SEM micrographs of the oxide scales on the air-side and fuel-side of the Al_2O_3-coated sample. After pre-oxidation, the uncoated air-facing side of the sample (see Fig. 6a) shows an oxide scale that is covering the surface, similar to the uncoated sample (see Fig. 2a), together with the presence of some small nodules that are around ~2 μm in thickness and still covered by the oxide scale. The fuel-side (see Fig. 6b) shows a surface that is fully covered with Al_2O_3.

After 3000 h of exposure, very few Fe_2O_3 nodules are present on the air-side (Fig. 6c). Closer examination uncovers small nodules that are still covered with the oxide, as observed after pre-oxidation. The nodule size (~2 μm) is similar to that observed after pre-oxidation (see Fig. 6a). The cross-section of the air-side (Fig. 6d) shows a thin (~200 nm) and homogeneous (Cr, Mn)$_3$O$_4$ protective spinel and the presence of small (Fe, Cr, Mn)$_3$O$_4$ nodules, as previously seen in the top-view image (see Fig. 2c) for uncoated samples. The plan-view of the fuel-side (Fig. 6e) shows a protective Al_2O_3 oxide scale covering the sample, identical to that observed after pre-oxidation (see Fig. 6b). However, small micro-cracks are visible on the sample surface after 3000 h of exposure. The top layer of the fuel-side (Fig. 6f) consists of a continuous Al_2O_3 oxide layer (~500 nm thick) and, closest to the metal, a thin Cr rich oxide scale (~150 nm in thickness). It is assumed that oxygen diffused through the micro-cracks and oxidised the steel underneath the protective Al_2O_3 layer. No signs of spallation of the oxide scale were recorded for the sample, indicating good adherence of the sputtered oxide. The desired phase for this application is α-Al_2O_3, as it has the lowest permeability to hydrogen [54–56]. Grazing Incidence X-ray Diffractogram (GI-XRD) confirms the presence of corundum type phase, corresponding to Cr_2O_3 and a spinel phase (Cr,Mn,Fe)$_3$O$_4$. No crystalline Al oxide was detected. Hence the layer is considered amorphous.

The Al_2O_3-coated sample on the fuel-side displays very few Fe_2O_3 nodules along the surface, indicating good protection against the dual-atmosphere effect. Previous research [57] has established the high density, low porosity, low number of defects and good stability of alumina.

Initial interactions of the Al coatings and Al_2O_3 coatings with the substrate

The thickness of the Al coating observed here (see Figs. 4f and 5f) does not match the initial thickness of the Al coating (see Table 2). To investigate this further, the initial stages of the interactions of the Al and Al_2O_3 coatings were investigated. From Fig. 7 it is clear that the observed coating thicknesses before exposure match well with the nominal thicknesses (see Table 2). The bottom part of Fig. 7 shows that after 5 h of pre-oxidation at 800 °C, the 1-μm-thick Al coating has shrunk to a thickness of approximately 500 nm. The thickness of the Al_2O_3 coating is unchanged.

The loss of Al is attributed to interdiffusion between the coating and the steel substrate. To quantify this, a line-scan analysis was conducted on the Al-coated 441 sample that was pre-oxidised for 5 h. The analysis revealed that after 5 h of pre-oxidation at 800 °C, Al had diffused into the alloy (to a depth of ~15 μm). Fig. 8 displays the line-scan data for the relevant species from the surface to the bulk. Beneath the Al rich surface layer, the Al concentration gradually decreases from 4% to the detection limit of the EDS. The EDS line-scan also indicates the presence of Fe within the top layer (at ~10 at%). The analysis was repeated twice to ensure reproducibility. This proves that Al diffuses inside the alloy during the pre-oxidation step. Due to the slow heating rate evaporation of metallic Al is considered unlikely but cannot be excluded (see Fig. 8).

Investigation of the conductivity of the alumina coatings

The electrical conductivity of the coated interconnects directly influences the final performance of a fuel cell. Therefore, the conductivity value must be kept as low as possible and should increase as little as possible over time. A value of <100 mΩ·cm^2 is commonly reported as an acceptable threshold for ASR [58]. Since Al_2O_3 is known to be a poor conductor [59–61], the oxide scale resistance of the Al- and Al_2O_3-coated samples were investigated at 600 °C in humid Ar − 5% H_2, to simulate the fuel-side atmosphere (see Fig. 9). The ASR of the uncoated sample was measured as a reference. The samples were exposed in Ar − 5% H_2 +3% H_2O for 1 week. The

Please cite this article as: Tomas M et al., Novel coatings for protecting solid oxide fuel cell interconnects against the dual-atmosphere effect, International Journal of Hydrogen Energy, https://doi.org/10.1016/j.ijhydene.2023.01.313

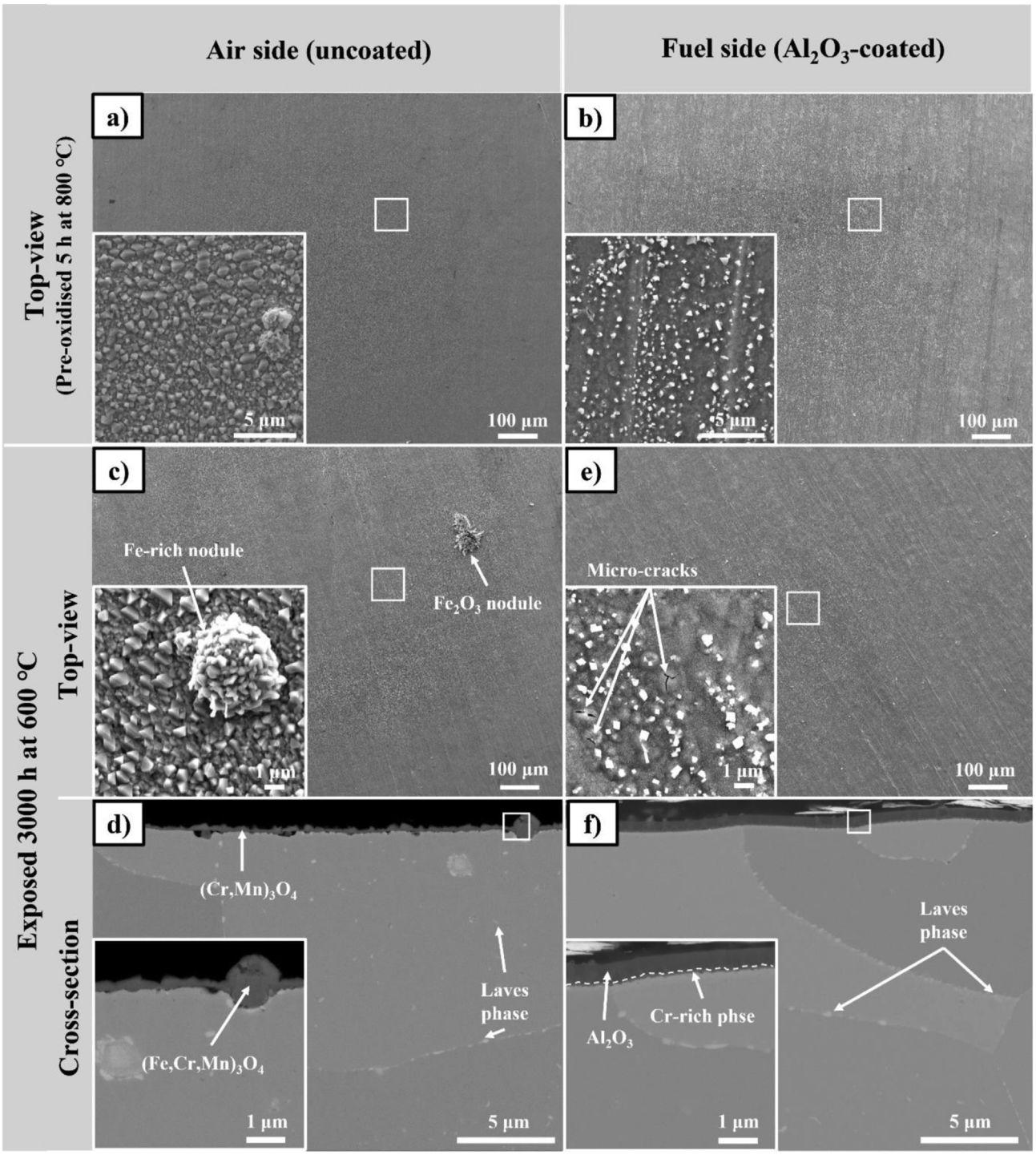

Fig. 6 – SEM micrographs representing: a) top-view of the air-side of the pre-oxidised sample; b) top-view of the fuel-side of the pre-oxidised sample; c) top-view of the air-side; d) cross-section of the air-side; e) top-view of the fuel-side; and f) cross-section of the fuel-side of the 441 Al_2O_3 (~500 nm)-coated sample exposed to the dual-atmosphere (Ar-5% H_2 + 3% H_2O// Air + 3% H_2O) for 3000 h at 600 °C. Inset: higher magnification of selected scale regions.

oxide layer formed at the air-side during exposure was ground off (the uncoated side of the sample) to minimize the contribution from that surface. For the uncoated material, a value of about 23 mΩ·cm^2 was recorded, while for the Al-coated samples, a value of about 75 mΩ·cm^2 was measured and for Al_2O_3-coated sample, a value of roughly 1 Ω·cm^2 was obtained, which is much higher than what is considered to be an acceptable ASR. Although it is an excellent barrier to hydrogen permeation, Al_2O_3 seems to be unsuitable for interconnect applications if anode-side contacting cannot be designed in a

Please cite this article as: Tomas M et al., Novel coatings for protecting solid oxide fuel cell interconnects against the dual-atmosphere effect, International Journal of Hydrogen Energy, https://doi.org/10.1016/j.ijhydene.2023.01.313

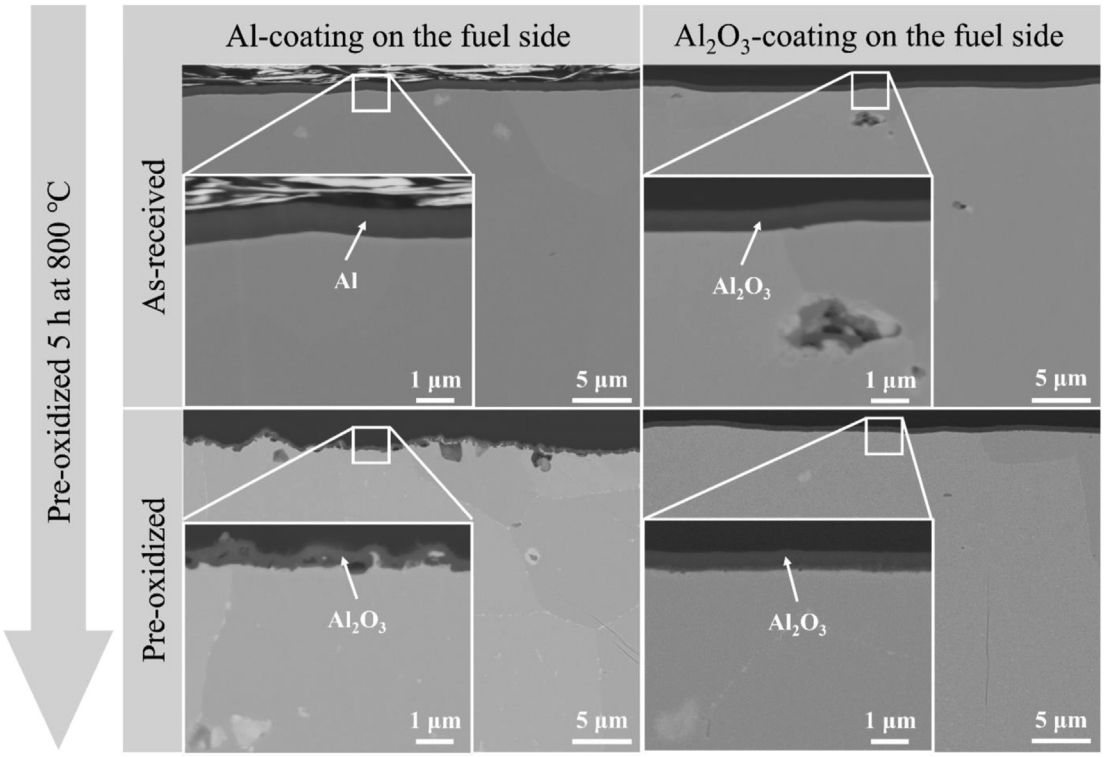

Fig. 7 – Effect of the pre-oxidation step on metallic Al coating. Top panel: As-received Al-coated and Al_2O_3-coated 441 steel. Bottom panel: The same surface after 5 h of pre-oxidation with up and down ramp rates of 1 °C/min in humid (3% water vapour) laboratory air at 800 °C.

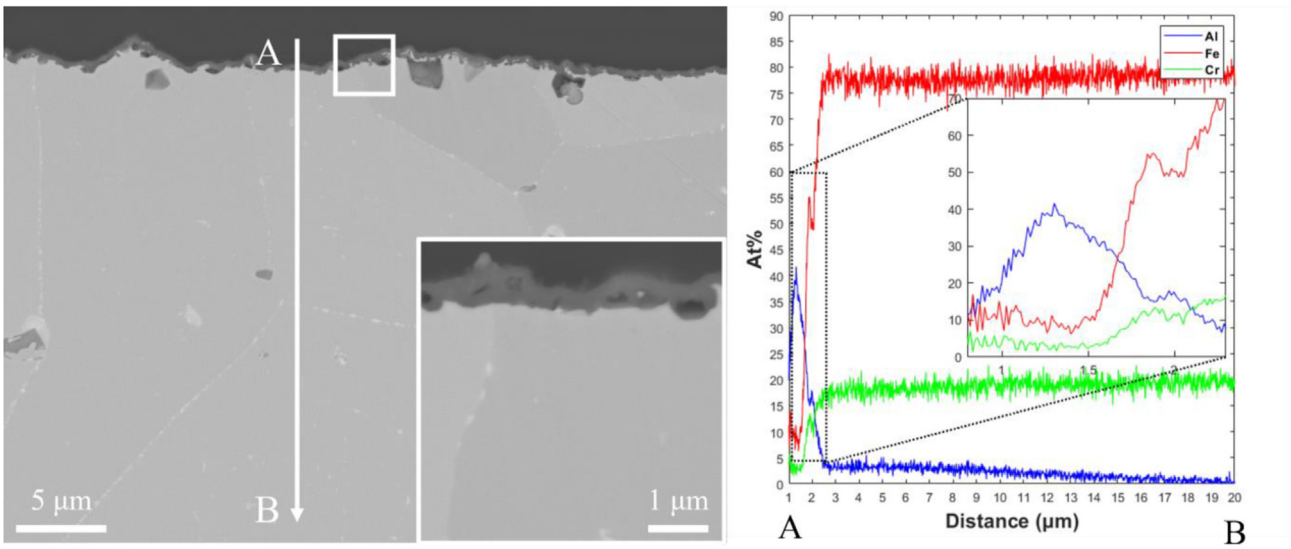

Fig. 8 – SEM micrograph representing the line-scan analysis used to determine the inter-diffusion of Al within the sample for an Al-coated 441 sample exposed for 5 h in humid air (3% water vapour) at 800 °C with up and down ramp rates of 1 °C/min.

way to circumvent the insulating Al_2O_3 layer. The 75 mΩ·cm^2 measured for the Al-coated sample are under the commonly cited target of 100 mΩ·cm^2, however, this value was obtained after 1 week and it is questionable to meet the target during long term operation. The fact that the value is much lower than Al_2O_3 is attributed in part to the lower thickness but mostly due to the fact that Fe is incorporated into the Al rich layer. An aliovalent ion such as Fe is expected to significantly improve the conductivity. Whether it is possible to further dope the Al rich layer in order to achieve lower ASR values without compromising the hydrogen barrier function needs to be studied further.

Please cite this article as: Tomas M et al., Novel coatings for protecting solid oxide fuel cell interconnects against the dual-atmosphere effect, International Journal of Hydrogen Energy, https://doi.org/10.1016/j.ijhydene.2023.01.313

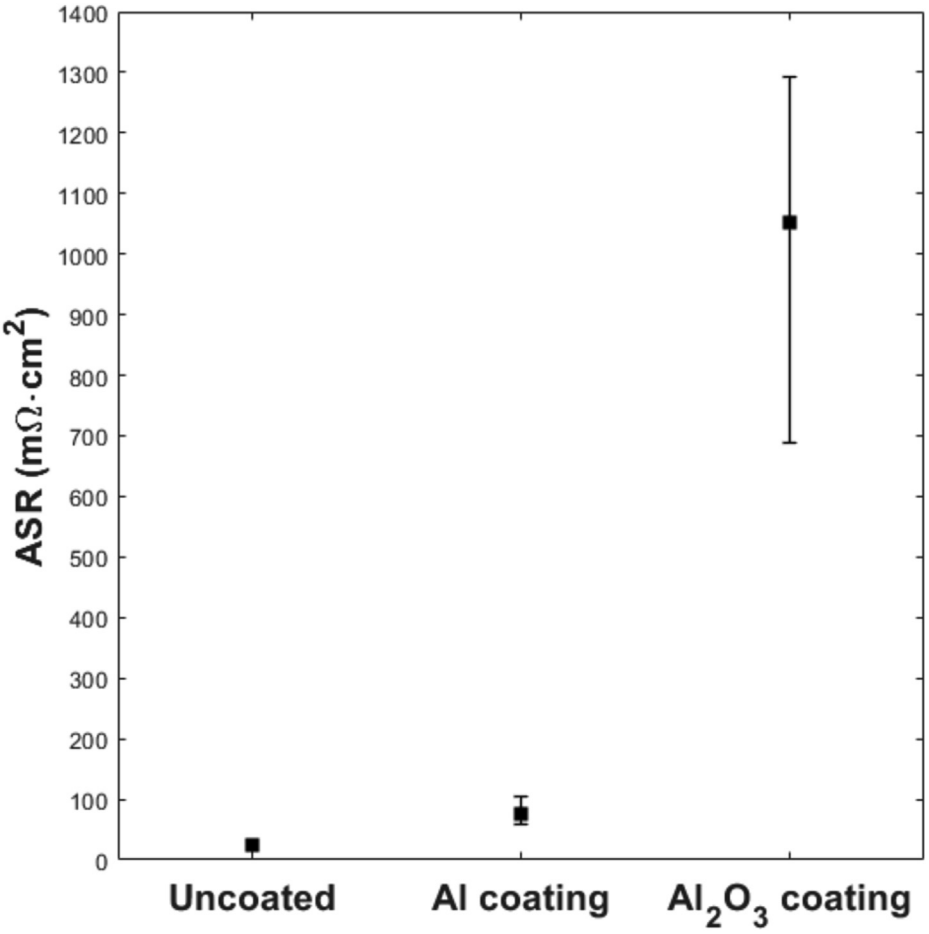

Fig. 9 – ASR measurements of uncoated, PVD Al-coated and PVD Al_2O_3-coated samples, exposed to Ar – 5% H_2 – 3% H_2O with a flow rate of 120 smL·min^{-1} for 168 h at 600 °C. The error bars represent the minimum and maximum measured values.

Conclusion

Air-side and fuel-side coatings have been studied in this work to evaluate their protective properties with respect to mitigating dual-atmosphere corrosion of FeCr steel at 600 °C. The main outcome is that coatings on the fuel-side seem to be more effective in reducing corrosion on the air facing side of the sample, than coatings on the air-side. However, coatings on the air-side are essential to reduce Cr(VI) evaporation in order avoid cathode poisoning. This works main findings are that.

- CeCo-coated samples on the air-side exhibit a more localised breakaway oxidation than uncoated samples;
- Metallic Al-coated samples exhibit excellent protection against hydrogen permeation, despite the initial breakaway oxidation that occurs during the pre-oxidation step;
- Al_2O_3-coated samples display the highest level of protection against the dual-atmosphere effect; and
- The combination of Ce/Co and Al coatings confers an excellent protection against the dual-atmosphere effect.

The metallic aluminium and Al_2O_3 coatings seem to be the best barriers against hydrogen permeation. However, ASR measurements, in particular of the Al_2O_3 coating show very poor conductivity, making its use as a coating for SOFC interconnects challenging.

Declaration of competing interest

The authors declare that they have no known competing financial interests or personal relationships that could have appeared to influence the work reported in this paper.

Acknowledgements

This work was conducted at the Swedish High Temperature Corrosion Centre (HTC) at Chalmers University of Technology. This work was performed in part at the Chalmers Material Analysis Laboratory, CMAL. The authors are grateful for

funding by the Swedish Energy Agency through grant 2015-009652.

Appendix A. Supplementary data

Supplementary data to this article can be found online at https://doi.org/10.1016/j.ijhydene.2023.01.313.

REFERENCES

[1] Powell M, et al. Demonstration of a highly efficient solid oxide fuel cell power system using adiabatic steam reforming and anode gas recirculation. J Power Sources 2012;205:377–84.
[2] Stambouli AB, Traversa EJR, reviews se. Solid oxide fuel cells (SOFCs): a review of an environmentally clean and efficient source of energy 2002;6(5):433–55.
[3] Niewolak L, et al. Mechanisms of oxide scale formation on ferritic interconnect steel in simulated low and high pO2 service environments of solid oxide fuel cells. Oxid Metals 2014;82(1):123–43.
[4] Horita T, et al. Accelerated degradation of SOFC cathodes by Cr vapors. In: Solid oxide fuel cells 11 (SOFC-XI); 2009. p. 2881–8.
[5] Stanislowski M, et al. Chromium vaporization from high-temperature alloys I. Chromia-forming steels and the influence of outer oxide layers 2007;154(4):A295–306.
[6] Hilpert K, et al. Chromium vapor species over solid oxide fuel cell interconnect materials and their potential for degradation processes 1996;143(11):3642–7.
[7] Zhang H, et al. Studies on elements diffusion of Mn/Co coated ferritic stainless steel for solid oxide fuel cell interconnects application. Int J Hydrogen Energy 2013;38(12):5075–83.
[8] Chen S, Jin X, Rong L. Improvement in high temperature oxidation resistance of 9% Cr ferritic–martensitic steel by enhanced diffusion of Mn. Oxid Metals 2016;85(1–2):189–203.
[9] Froitzheim J, Svensson J-E. Multifunctional nano-coatings for SOFC interconnects. ECS Trans 2011;35(1):2503.
[10] Hou P, Stringer J. The effect of reactive element additions on the selective oxidation, growth and adhesion of chromia scales. Mater Sci Eng 1995;202(1–2):1–10.
[11] Canovic S, et al. Oxidation of Co-and Ce-nanocoated FeCr steels: a microstructural investigation. Surf Coating Technol 2013;215:62–74.
[12] Falk-Windisch H, et al. Co-And Ce/Co-coated ferritic stainless steel as interconnect material for intermediate temperature solid oxide fuel cells. J Power Sources 2017;343:1–10.
[13] Froitzheim J, et al. Long term study of Cr evaporation and high temperature corrosion behaviour of Co coated ferritic steel for solid oxide fuel cell interconnects. J Power Sources 2012;220:217–27.
[14] Alnegren P, et al. Severe dual atmosphere effect at 600 C for stainless steel 441. J Power Sources 2016;301:170–8.
[15] Gunduz KO, et al. The effect of hydrogen on the breakdown of the protective oxide scale in solid oxide fuel cell interconnects. Corrosion Sci 2021;179:109112.
[16] Sabioni ACS, et al. Comparative study of high temperature oxidation behaviour in AISI 304 and AISI 439 stainless steels. Mater Res 2003;6(2):179–85.
[17] Yang Z, et al. Anomalous corrosion behavior of stainless steels under SOFC interconnect exposure conditions. Electrochem Solid State Lett 2003;6(10):B35.
[18] Yang Z, et al. Oxidation behavior of ferritic stainless steels under SOFC interconnect exposure conditions. J Electrochem Soc 2004;151(12):B669.
[19] Alnegren P, et al. Temperature dependence of corrosion of ferritic stainless steel in dual atmosphere at 600–800 C. J Power Sources 2018;392:129–38.
[20] Kurokawa H, Kawamura K, Maruyama T. Oxidation behavior of Fe–16Cr alloy interconnect for SOFC under hydrogen potential gradient. Solid State Ionics 2004;168(1–2):13–21.
[21] Rufner J, et al. Oxidation behavior of stainless steel 430 and 441 at 800 C in single (air/air) and dual atmosphere (air/hydrogen) exposures. Int J Hydrogen Energy 2008;33(4):1392–8.
[22] Stygar M, et al. Oxidation properties of ferritic stainless steel in dual Ar–H2–H2O/air atmosphere exposure with regard to SOFC interconnect application. Solid State Ionics 2014;262:449–53.
[23] Horita T, et al. Oxide scale formation and stability of Fe–Cr alloy interconnects under dual atmospheres and current flow conditions for SOFCs. J Electrochem Soc 2006;153(11):A2007.
[24] Horita T, et al. Evaluation of Fe-Cr alloys as interconnects for reduced operation temperature SOFCs. J Electrochem Soc 2003;150(3):A243.
[25] Gagliani L, et al. The influence of humidity content on ferritic stainless steels used in solid oxide fuel cell under dual atmosphere conditions at 600° C. ECS Trans 2021;103(1):1809.
[26] Nakagawa K, Matsunaga Y, Yanagisawa T. Corrosion behavior of ferritic steels on the air sides of boiler tubes in a steam/air dual environment. Mater A T High Temp 2003;20(1):67–73.
[27] Ardigo M, et al. Dual atmosphere study of the K41X stainless steel for interconnect application in high temperature water vapour electrolysis. Int J Hydrogen Energy 2015;40(15):5305–12.
[28] Goebel C, et al. The effect of pre-oxidation parameters on the corrosion behavior of AISI 441 in dual atmosphere. Int J Hydrogen Energy 2018;43(31):14665–74.
[29] Li J, et al. Investigation of anomalous oxidation behavior of SUS430 alloy in solid oxide fuel cell dual atmosphere. J Electrochem Soc 2017;164(14):C945.
[30] Zhao Y, Fergus J. Oxidation of alloys 430 and 441 in SOFC dual atmospheres: effects of flow rate and humidity. J Electrochem Soc 2011;159(3):C109.
[31] Skilbred AWB, Haugsrud R. The effect of dual atmosphere conditions on the corrosion of Sandvik Sanergy HT. Int J Hydrogen Energy 2012;37(9):8095–101.
[32] Reisert M, Aphale A, Singh P. Observations on accelerated oxidation of a ferritic stainless steel under dual atmosphere exposure conditions. In: Energy technology 2019. Springer; 2019. p. 273–81.
[33] Amendola R, et al. Oxidation behavior of coated and preoxidized ferritic steel in single and dual atmosphere exposures at 800 C. Surf Coating Technol 2012;206(8–9):2173–80.
[34] Reisert M, et al. Corrosion of chromia-forming and alumina-forming ferritic stainless steels under dual atmosphere exposure conditions. J Electrochem Soc 2021;168(11):111506.
[35] Reisert M, Aphale AN, Singh P. The effects of dual atmosphere exposure duration and temperature on the growth of iron oxide on ferritic stainless steels. ECS Trans 2020;98(1):35.
[36] Essuman E, et al. The effect of water vapor on selective oxidation of Fe–Cr alloys. Oxid Metals 2008;69(3):143–62.
[37] Hammer J, et al. The oxidation of ferritic stainless steels in simulated solid-oxide fuel-cell atmospheres. Oxid Metals 2007;67(1):1–38.

Please cite this article as: Tomas M et al., Novel coatings for protecting solid oxide fuel cell interconnects against the dual-atmosphere effect, International Journal of Hydrogen Energy, https://doi.org/10.1016/j.ijhydene.2023.01.313

[38] Goebel C, et al. The influence of different factors on the dual atmosphere effect observed for AISI 441 interconnects used in solid oxide fuel cells. ECS Trans 2019;91(1):2261.
[39] Skilbred AWB, Haugsrud R. The effect of water vapour on the corrosion of Sandvik Sanergy HT under dual atmosphere conditions. Oxid Metals 2013;79(5):639–54.
[40] Mikkola J, et al. Protective coatings for ferritic stainless steel interconnect materials in high temperature solid oxide electrolyser atmospheres. Energies 2022;15(3):1168.
[41] Molin S, et al. Effective yttrium based coating for steel interconnects of solid oxide cells: corrosion evaluation in steam-hydrogen atmosphere. J Power Sources 2019;440:226814.
[42] Froitzheim J, et al. Anode side diffusion barrier coating for solid oxide fuel cells interconnects. 2010.
[43] Garcia-Fresnillo L, et al. Oxidation behaviour and phase transformations of an interconnect material in simulated anode environment of intermediate temperature solid oxide fuel cells. Mater A T High Temp 2017;34(1):61–77.
[44] Nielsen K, et al. Testing of Ni-plated ferritic steel interconnect in SOFC stacks. Fuel Cell 2006;6(2):100–6.
[45] Leah R, Selcuk A. Interconnect for a low temperature solid oxide fuel cell. E.P. Office. United Kingdom. Ceres Limited Property Co Ltd. EP3256617B1; 2019.
[46] Froitzheim J, et al. Investigation of chromium volatilization from FeCr interconnects by a denuder technique. J Electrochem Soc 2010;157(9):B1295–300.
[47] Reisert M, et al. Preformed oxide scale chemistry and its influence on local metal loss during dual atmosphere corrosion. In: TMS 2020 149th annual meeting & exhibition supplemental proceedings. Springer; 2020.
[48] Nemanič V. Hydrogen permeation barriers: basic requirements, materials selection, deposition methods, and quality evaluation. Nuclear Materials and Energy 2019;19:451–7.
[49] Charles H, Charles H. Hydrogen permeation barrier coatings. 2008.
[50] Jung I-H. Critical evaluation and thermodynamic modeling of the Mn–Cr–O system for the oxidation of SOFC interconnect. Solid State Ionics 2006;177(7):765–77.
[51] Kurokawa H, et al. Hydrogen permeation through Fe-16Cr alloy interconnect in atmosphere simulating SOFC at 1073 K. J Electrochem Soc 2004;151(8):A1264.
[52] Stanislowski M, et al. Reduction of chromium vaporization from SOFC interconnectors by highly effective coatings. J Power Sources 2007;164(2):578–89.
[53] Falk-Windisch H, et al. Chromium vaporization from mechanically deformed pre-coated interconnects in Solid Oxide Fuel Cells. J Power Sources 2015;297:217–23.
[54] Roberts RM, et al. Hydrogen permeability of sintered aluminum oxide. J Am Ceram Soc 1979;62(9-10):495–9.
[55] Shirasaka H, et al. Analysis of gas permeability of porous alumina powder compacts. Journal of Asian Ceramic Societies 2013;1(4):368–73.
[56] Serra E, et al. Hydrogen permeation measurements on alumina. J Am Ceram Soc 2005;88(1):15–8.
[57] Ruppi S. Deposition, microstructure and properties of texture-controlled CVD α-Al2O3 coatings. Int J Refract Metals Hard Mater 2005;23(4–6):306–16.
[58] Piccardo P, et al. ASR evaluation of different kinds of coatings on a ferritic stainless steel as SOFC interconnects. Surf Coating Technol 2007;202(4):1221–5.
[59] Arizumi T, Tani S. On the electrical conductivity of alumina. J Phys Soc Jpn 1950;5(6):442–7.
[60] Cohen J. Electrical conductivity of alumina. Am Ceram Soc Bull 1959;38(9):441–6.
[61] Schemmel R, et al. Electrical properties of a polycrystalline alumina sample. Richland, WA (United States): Hanford Engineering Development Lab.; 1972.

Please cite this article as: Tomas M et al., Novel coatings for protecting solid oxide fuel cell interconnects against the dual-atmosphere effect, International Journal of Hydrogen Energy, https://doi.org/10.1016/j.ijhydene.2023.01.313